

Chapter 1

Raman Spectroscopy of Monolayer and Multilayer Graphenes



Jiang-Bin Wu, Miao-Ling Lin, and Ping-Heng Tan

Abstract The discovery of monolayer graphene in 2004 has triggered a great effort to investigate the fundamental properties and applications of all two-dimensional materials (2DMs). Monolayer graphene (1LG) can be stacked layer by layer in a particular way (AB, ABC and twist) to form multilayer graphene (MLG), whose properties vary according to the stacking. Raman spectroscopy is a useful tool to reveal the chemical and physical properties of graphene materials. In this chapter, we review the systematic development of the Raman spectroscopy of pristine 1LG and MLG. The essential Raman scattering processes of the entire first and second order modes in intrinsic 1LG are addressed in detail. We further introduce the concept of double resonance Raman scattering in graphene. Moreover, a series of works on the shear (C), layer-breathing (LB) and 2D modes of MLGs with different stacking orders are discussed. Finally, various types of resonance Raman spectroscopy of 1LG and MLG are also presented. The Raman spectroscopy of graphene materials can serve as a typical example in studying the Raman spectroscopy of other 2DMs and introducing the fundamental physical concepts for 2DMs.

The original version of this chapter was revised. A correction to this chapter is available at https://doi.org/10.1007/978-981-13-1828-3_12

J.-B. Wu · M.-L. Lin

State Key Laboratory of Superlattices and Microstructures, Institute of Semiconductors, Chinese Academy of Sciences, Beijing, China

College of Materials Science and Opto-Electronic Technology, University of Chinese Academy of Science, Beijing, China

P.-H. Tan (✉)

State Key Laboratory of Superlattices and Microstructures, Institute of Semiconductors, Chinese Academy of Sciences, Beijing, China

Center of Materials Science and Opto-Electronics Engineering & CAS Center of Excellence in Topological Quantum Computation, University of Chinese Academy of Sciences, Beijing, China
e-mail: phtan@semi.ac.cn

© Springer Nature Singapore Pte Ltd. 2019

P.-H. Tan (ed.), *Raman Spectroscopy of Two-Dimensional Materials*, Springer Series in Materials Science 276, https://doi.org/10.1007/978-981-13-1828-3_1

1.1 Introduction

There are many members in the two-dimensional (2d) material family. Monolayer graphene (1LG) is a truly 2d system; the atoms in one plane are connected via strong covalent bonds, forming sp^2 carbon hexagonal networks [1]. 1LG can be stacked layer by layer in the Bernal (AB) or rhombohedral (ABC) manner via van der Waals (vdW) coupling to form multilayer graphene (MLG). AB-stacked and ABC-stacked MLG are denoted AB-MLG and ABC-MLG, respectively. Each N -layer graphene (N LG) exhibits distinct electronic band structure dependent on the layer number N , interlayer coupling and stacking order [2]. When the physical properties related to the interlayer coupling and stacking order are discussed in this chapter for N LG, N is assumed to be no less than the smallest layer number of the corresponding MLG; thus, $N > 1$ for AB-stacked N LG (AB- N LG), and $N > 2$ for ABC-stacked N LG (ABC- N LG). High-quality N LG flakes can be produced by several methods, such as micromechanical exfoliation (ME), chemical vapour deposition (CVD) and epitaxial growth from the SiC surface [3–5]. Graphene materials exhibit many remarkable properties, making them the ideal materials for next-generation nanoscale devices [6–9]. On the other hand, 1LG and MLG are usually the typical essential building blocks for vdW heterostructures (vdWHs), which can be formed by vertically stacking various 2d materials (2DMs) via vdW coupling but without any constraints of lattice matching and fabrication compatibility, [7, 10] offering significant opportunities for designing functionalities [7, 8]. The graphene materials in vdWHs are usually employed as electrodes to form various high-performance devices, such as field-effect tunnelling transistors, logic transistors, photovoltaics and memory devices [7, 8, 10]. All the facts stated above imply that graphene materials can serve as a typical prototype to introduce the physical properties and fundamental concepts of 2DMs.

Raman spectroscopy has historically played an important role in nondestructively characterizing the lattice structure and electronic, optical and phonon properties of graphene materials with high resolution [9, 11, 12]. N LG exhibits N -dependent and stacking-orientation dependent Raman features, providing information on the phonon properties and on their unique band structures [13, 14]. In addition, quantum interference effects can serve as the main factor to modify the Raman intensity of N LG [15–17]. Therefore, it is easy to determine the physical properties of graphene materials and the performance mechanism in graphene-based devices using Raman spectroscopy [9].

In this chapter, we review the systematic development of Raman spectroscopy of 1LG and MLG. We further introduce the concept of double resonance Raman scattering in graphene in detail. A series of studies about the shear (C), layer-breathing (LB) and 2D modes of MLGs with different stacking orders are discussed. The shear modes are usually referred to as the C modes in MLGs because it provides a direct measurement of the interlayer *Coupling*. Various types of resonance Raman spectroscopy of 1LG and MLG are also presented. A more systematical review on

the developments in the Raman spectroscopy of graphene-based materials from both fundamental research and practical (i.e., device applications) perspectives can be found in our recent review paper [9].

1.2 Raman Spectroscopy of Monolayer Graphene

1.2.1 Band Structure of Monolayer and Multilayer Graphenes

There are two inequivalent carbon atoms, A and B, in a unit cell of 1LG, each forming a triangular in-plane network. The distance between these two atoms, also called the length of the carbon-carbon covalent bond, is 0.142 nm, leading to a 0.246 nm lattice constant, as shown in Fig. 1.1a. MLG is a layered structure obtained from 1LG by stacking in the out-of-plane direction (c -axis) with an interlayer distance of 0.334 nm. AB stacking is the most common and stable stacking in MLG, in which the two adjacent graphene layers are vertically stacked with 60° rotation. Thus, the vacant centres of the hexagons on one layer are occupied by the carbon atoms at hexagonal corner sites on the adjacent layers from the top view, as shown in Fig. 1.1b. The two next nearest layers are in superposition from the top view in AB-stacked *N*LG. Moreover, the unit cell of graphite can also be shown as Fig. 1.1b, whose lattice constants are $a = 0.246$ nm and $c = 0.67$ nm. The reciprocal space of 1LG is a plane, as shown in Fig. 1.1c. The high symmetry points within the Brillouin zone (BZ) of 1LG are also shown in Fig. 1.1c, with the Γ point at the zone centre, M points in the middle of the hexagonal sides, and K and K' points at the corners of the hexagons. The K and K' points are inequivalent.

Graphene is a zero-gap semi-metal with a linear electronic band structure, which causes its unique optical properties from the terahertz to the visible range [19]. Furthermore, any laser excitation from the visible to the ultraviolet can induce a quantum interference effect in the Raman scattering process, making the Raman spectrum of graphene remarkable [15]. As N increases, *N*LG exhibits significant N -dependent electronic band structures due to the interlayer vdW coupling and different symmetries [2]. Micromechanical exfoliation was the first method used to produce *N*LG flakes with high quality. The exfoliated graphene flakes are usually deposited onto a Si/SiO₂ substrate with a specific thickness (90 or 300 nm), as shown in Fig. 1.1d, which makes the graphene visible and enhances Raman signals of graphene due to the optical interference effect in the air/*N*LG/SiO₂/Si multilayered structure [17, 20, 21]. Figure 1.1e–h shows the linear band structure of 1LG and the corresponding band structures of AB-2LG, -3LG and -4LG. The difference in the band structures in *N*LG can be reflected in their peculiar Raman features [9, 13]. Thus, Raman spectroscopy can be used to probe the band structure of 2LG [14] and to identify 1–4LG [22].

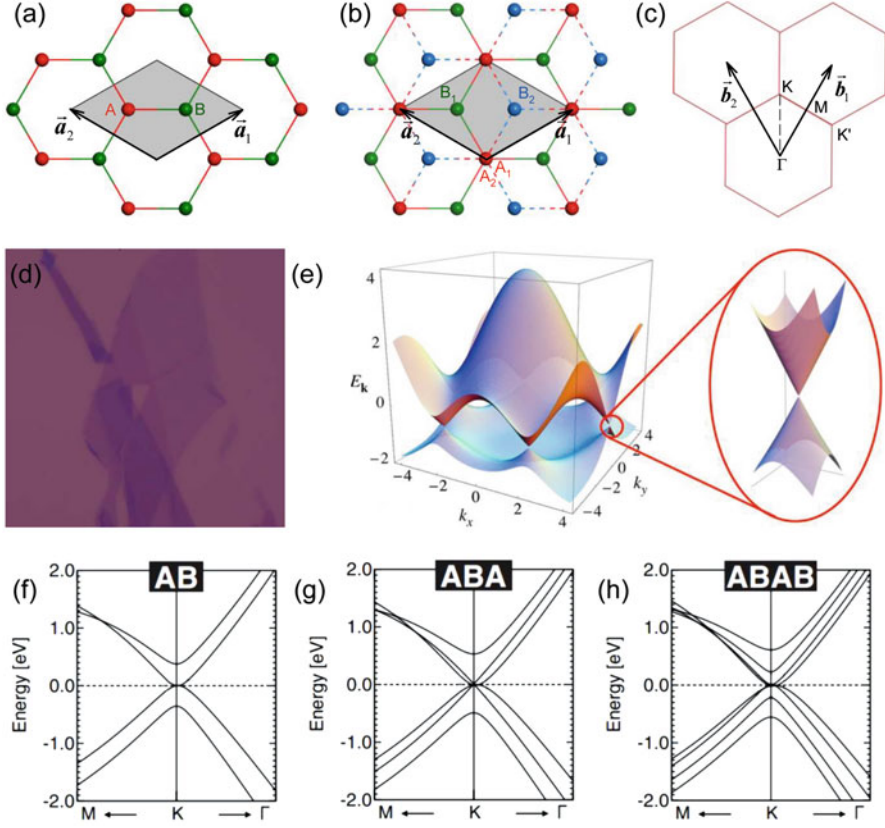


Fig. 1.1 (a) A top view of the unit cell of a 1LG lattice. (b) A top view of AB-stacked 2LG. (c) The unit cell in reciprocal space of 1LG. The primitive vectors and high symmetry points are shown. (d) Optical image of exfoliated graphene flakes on a Si/SiO₂ substrate. (e) Band structure of 1LG. (Reproduced with permission from Ref. [18]). Band structure of AB-stacked 2LG (f), 3LG (g) and 4LG (h) in the vicinity of K. (Reproduced with permission from Ref. [2])

1.2.2 Phonon Dispersion and the Raman Spectrum of Graphene

The phonon modes (lattice vibrations) are usually presented by the irreducible representation based on the symmetry group of the crystals, which are essential to the interpretation of Raman spectra. The point group symmetries of 1LG and graphite are both D_{6h} . As two and four atoms are in the unit cells of 1LG and graphite, six and twelve phonon modes are expected, respectively. Thus, the lattice vibrations of 1LG and graphite at Γ can be expressed as $\Gamma_{1LG} = A_{2u} + B_{2g} + E_{1u} + E_{2g}$ and $\Gamma_{bulk} = 2(A_{2u} + B_{2g} + E_{1u} + E_{2g})$ [25]. One A_{2u} mode and one doubly degenerate E_{1u} mode are the three acoustic modes in 1LG and bulk. As for the optical

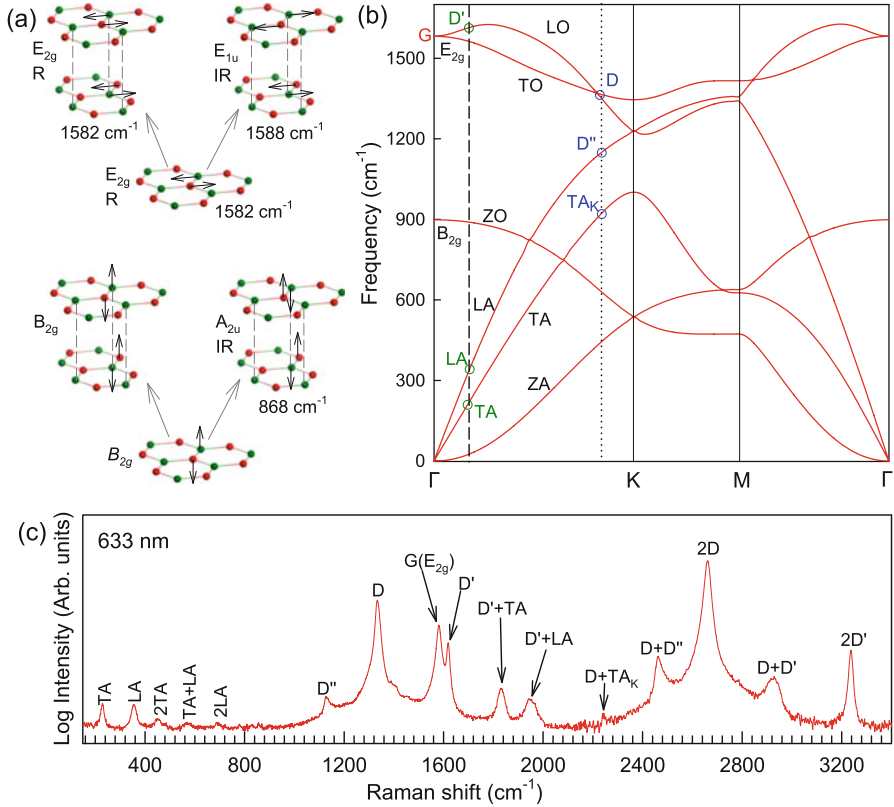


Fig. 1.2 (a) Phonon-displacement pattern at the Γ -point for graphene and graphite. Long arrows show how each phonon mode in graphene gives rise to two phonon modes of graphite. (b) The solid curves represent the dispersion of phonon modes in graphene calculated by density functional perturbation theory. (Reproduced with permission from Ref. [23]). The attribution of each branch is labelled. (c) 633 nm excited Raman spectrum under excitation at 633 nm of a graphite whisker, which can be considered as the assembly of individual 1LG. (Reproduced with permission from Ref. [24])

phonon, 1LG contains the doubly degenerate in-plane mode, E_{2g} , and one out-of-plane mode, B_{2g} , as shown in Fig. 1.2a. In graphite, several Davydov doublets are present because the two graphene layers in the unit cell of graphite are inequivalent, [11, 12] *e.g.*, the E_{2g} mode in 1LG generates an infrared-active mode, E_{1u} , and a Raman-active (R) mode, E_{2g} , in graphite, and the B_{2g} mode in 1LG divides into an infrared-active (IR) mode, A_{2u} , and an inactive mode, B_{2g} , in graphite, as shown in Fig. 1.2a. The corresponding frequencies and atomic displacements are also depicted. In graphite, the E_{2g} mode at $\sim 1582 \text{ cm}^{-1}$ is the characteristic peak of graphene-related materials, named the G mode. The remaining E_{2g} and one B_{2g} mode are the C and LB modes, corresponding to the in-plane and out-of-plane interlayer vibration of the rigid atom layers, respectively [26, 27]. Due to the weak

interlayer coupling, the peak position of the C mode (Pos(C)) is very low, located at 43.5 cm^{-1} [26, 28]. The LB modes are silent and can not be observed in the Raman spectrum. Pos(LB) can be estimated to be $\sim 125.3 \text{ cm}^{-1}$ based on the experimental Pos(LB) in twisted MLG [27].

The phonon dispersions of 1LG calculated by density functional perturbation theory (DFPT) within the local density approximation are shown in Fig. 1.2b [23]. There are three acoustic branches and three optical branches in 1LG inherited from the six vibrational modes at the Γ point. The in-plane longitudinal acoustic (LA) and transverse acoustic (TA) branches have linear dispersion and higher frequencies than the out-of-plane acoustic (ZA) mode around Γ . The strong in-plane C-C bonds give large slopes of the LA (21.36 km/s) and TA (13.79 km/s) branches, leading to the high in-plane sound velocity of graphene and thus the ultra-high thermal conductivity [29]. The three optical branches: in-plane longitudinal optical (LO), in-plane transverse optical (TO) and out-of-plane optical (ZO) branches, correspond to the irreducible representations (Fig. 1.2a) E_{2g} (LO and TO) and B_{2g} (ZO) at Γ , respectively. The LO and TO branches split in frequency when the wave vector is away from Γ , and the frequency of the TO branch monotonically decreases along Γ -K. The phonon dispersions of solid materials are usually experimentally detected via inelastic X-ray, neutron scattering and high-resolution electron energy-loss spectroscopy [30, 31].

Figure 1.2c shows the Raman spectra of the graphite whisker in the region of $150\text{--}3400 \text{ cm}^{-1}$ under 633 nm excitation [24]. The spiral structure and cone tip of the graphite whisker suggest the existence of a twist angle between adjacent layers in the whisker, leading to weaker interlayer coupling compared to graphite. Thus, the graphite whisker can be considered as the assembly of individual 1LG units. Therefore, graphite whiskers can be considered as a prototype to show the abundant Raman modes that should be observed in 1LG [9]. Indeed, many weak first- and second-order Raman modes have been revealed in the Raman spectrum, as indicated in Fig. 1.2c. In principle, Raman spectroscopy can usually be used to probe the phonon modes in the BZ centre. Indeed, the G peak corresponds to the E_{2g} mode at Γ , located at $\sim 1582 \text{ cm}^{-1}$. The other Raman peaks observed in graphite whiskers or 1LG should correspond to phonons away from Γ . The observation of these phonons can be attributed to double resonance (DR) or triple resonance (TR) Raman processes in 1LG, as depicted in Fig. 1.3.

1.2.3 Double and Triple Resonance Raman Processes in Graphene

A resonance Raman process occurs when the excitation energy is chosen to match or nearly match an optical transition bandgap of the crystal, and the Raman intensity can be enhanced by 2 to 6 orders of magnitude. Because the two linear electronic bands of intrinsic 1LG cross at the Fermi energy, an incoming photon with energy

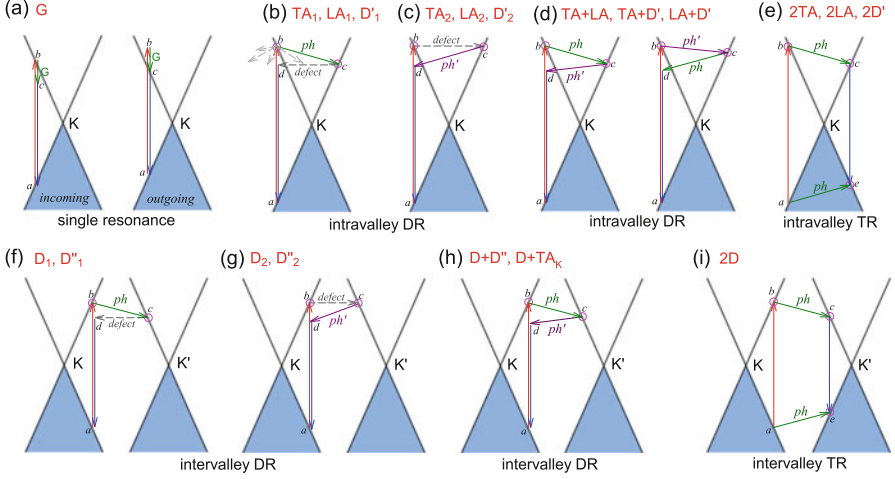


Fig. 1.3 (a) Incoming and outgoing single resonance processes of the G mode in 1LG. (b-i) Resonance processes of dispersive Raman modes in 1LG, including an electron-hole pair excited by an incident laser photon, inelastic scattering of the electron and hole by phonon emission/absorption, and the elastic scattering of the electron mediated by the defect, and recombination of the electron-hole pair. (b-d) The intravalley double resonance processes. (e) An intravalley triple resonance process. (f-h) The inner intervalley double resonance processes. (i) An inner intervalley triple resonance process. The Raman modes in graphite whiskers activated by each resonance process are labelled accordingly in each panel. (Reproduced with permission from Ref. [9])

ε_L can always excite a resonant transition from the state in the valence band to another state in the conduction band to generate an electron-hole pair. The excited electron can be scattered by the E_{2g} phonons to recombine with a hole, satisfying the incoming single resonance process. The outgoing single resonance process can also be satisfied for the G mode of 1LG. Both resonance processes are shown in Fig. 1.3a. The excited electron can also be scattered by phonons of an arbitrary wave vector, as shown in Fig. 1.3b by the dashed arrows. The scattering probability, however, will be particularly high if the phonon scatters the electron from one real electronic state b into another real state c . Such one-phonon first-order Raman scattering is forbidden by selection rules. However, the above scattered electron in state c can be scattered back to state d with the same wave vector as state b by crystal defects, which then leads to emission of a photon through recombination with a hole in the initial state. The above resonance process is one-phonon DR Raman scattering, in which the two events consist of one inelastic scattering event by emitting a phonon and one elastic scattering event by crystal defects. The two scattering processes can also start from an elastic scattering event followed by an inelastic scattering event, shown in Fig. 1.3c. If the elastic scattering of defects is displaced by another inelastic phonon scattering, the process becomes two-phonon DR Raman scattering, as illustrated in Fig. 1.3d. Further, if the valence and conduction bands are almost mirror bands, a triple resonance (TR) Raman process can occur. For

example, for the special case of 1LG, as shown in Fig. 1.3e, the electron-hole generation is a resonance process, and both electron and hole scattering will be resonant. Finally, the electron-hole recombination will also be resonant. Therefore, for the TR Raman process, all steps in the normal double resonance process become resonant [9].

The resonance processes in Fig. 1.3b–e are intravalley double resonance processes because two resonant electronic states are connected within the same Dirac cones at the K point (or the K' point) of 1LG. Instead, if the resonance process connects two associated resonant electronic states within the two inequivalent Dirac cones at the K and K' points of 1LG, the corresponding double resonance mechanism is called an intervalley process. By analogy to the intravalley DR and TR processes in Fig. 1.3b–e, the intervalley DR and TR processes also occur, [9] as shown in Fig. 1.3f–i. The double resonance processes in Fig. 1.3 only depict the incoming resonance process. After a careful analysis, there are two inequivalent DR processes for the fundamental and combination Raman modes mediated by the scattering of electrons, and there is only one double resonant process for the overtone mediated by the scattering of electrons [32]. It should be noted that the inelastic scattering of the hole by phonon emission/absorption and elastic scattering of the hole mediated by the defect can also be involved in the DR Raman process [33].

In principle, many different initial electronic states around the Dirac point and phonons with different symmetries and wave vectors can satisfy the DR conditions. However, considering (1) the existence of singularities in the density of phonon states that satisfy the DR condition, (2) the angular dependence of the electron-phonon scattering matrix elements, and (3) destructive interference effects when the Raman transition probability is calculated, only a few specific DR processes contribute to the observed Raman modes. Because there are two inequivalent DR Raman processes for both intravalley and intervalley DR Raman processes, each ε_L can select two phonon wave vectors for the fundamental and combination modes and one phonon wave vector for the overtones near the Γ and K points, respectively. Therefore, both the fundamental modes and the combination modes activated by the DR Raman process can be fitted by two Lorentzian peaks, while the overtone only exhibits a single Lorentzian peak [9, 24, 34].

Because the phonon energy in 1LG is much smaller than ε_L , for each ε_L , the phonons with almost equal wave vectors at different branches of the phonon dispersion curves can be probed by the DR Raman process. These are linked by the vertical dashed and dotted lines close to the Γ and K points, respectively, for the intravalley and intervalley DR Raman processes in Fig. 1.2b. Moreover, for the intervalley process, just the inner processes are shown in Fig. 1.3. The outer process can also exist to satisfy the DR conditions. The inner processes correspond to the phonon along the K- Γ line, while the outer processes correspond to the phonon along the K-M line. The most intense contribution to both the D and 2D intensity is due to phonons along the high-symmetry direction K- Γ line (inner phonons), according to the numerical calculation [33].

The observed Raman spectra in Fig. 1.2b can be well understood by the DR and TR Raman processes, as addressed above. The D (D'') peak is the phonon at the TO (LA) branch around the Brillouin zone corner K activated by a defect in the DR Raman process [32, 35]. The 2D peak is the overtone of the D peak, in which momentum conservation is satisfied by two phonons with opposite wave vectors. Thus, no defects are required for their activation, and these peaks are always present in the pristine 1LG. The DR Raman process can also involve two phonons from different branches, making the combination modes observable, such as $D + D''$ and $D + TA_K$ [9]. The $D + D''$ mode is assigned as a combination mode of a D mode from the TO phonon branch and a D'' mode belonging to the LA branch near the K point, seen at $\sim 1,100 \text{ cm}^{-1}$ [33, 36, 37]. The $D + TA_K$ mode is assigned as a combination mode of a D phonon and a phonon belonging to the TA branch near the K point [33]. All the DR-related modes mentioned above occur between two different valleys (K and K'). These intervalley DR processes involve the phonons near the K point as linked by the dotted line in Fig. 1.2b. The DR Raman process can also occur within the same valley, that is, connecting two points belonging to the same Dirac cone around K (or K'). Such an intravalley DR process associated with the LO (D') phonon near Γ and a defect gives the so-called D' peak, whose overtone is $2D'$ [34, 38]. The LA and TA phonons near Γ can also be activated by the defect to form LA and TA peaks in the Raman spectra, respectively, whose overtones are $2TA$ and $2TA$. The typical intravalley combination modes are $D' + TA$ and $D' + LA$. The LA and TA peaks can also be combined to form the LA + TA peak. All the above intravalley DR Raman modes (i.e., LA, TA, $D' + TA$, $D' + LA$ and LA + TA) associated with LA and TA phonons have been observed in the Raman spectra of a graphite whisker [24]. These intravalley DR processes involve the phonons near Γ , as linked by the dashed line in Fig. 1.2b.

For the DR or TR Raman processes, as depicted in Fig. 1.3, the wave vector of the involved phonons is determined by ε_L . Thus, the peak position of the corresponding Raman modes is dependent on ε_L . The dispersion for the 2D mode is almost linear with ε_L , with a slope of $\sim 100 \text{ cm}^{-1}/\text{eV}$, due to the linear band structure and the almost linear dispersion of the TO branch near K point. By neglecting the phonon energy, the dispersion slope of the frequency of the combination mode of phonon mode 1 (ph_1) and phonon mode 2 (ph_2) can be estimated as $(v_q^{ph_1} + v_q^{ph_2})/v_f$, where $v_q^{ph_1}$ and $v_q^{ph_2}$ are the phonon group velocity of ph_1 and ph_2 and $v_f = 10^6 \text{ m/s}$ is the Fermi velocity of 1LG. Thus, by detecting the DR modes with multi-wavelength Raman spectroscopy, the dispersion of the LO, TO, LA and TA branches can be observed [32–34]. Furthermore, the physical properties related to these branches, such as the Kohn anomaly [40], can be obtained. The doublet asymmetric profile in fundamental and combination peaks can be confirmed by the D mode of disordered 1LG, as shown in Fig. 1.4c. Obviously, the D peak can be fitted by two peaks, the D_1 and D_2 peaks. The D_1 peak is from the process plotted in Fig. 1.3f, and the D_2 peak is from the process plotted in Fig. 1.3g. The overtone modes, such as 2D and $2D'$, give a symmetric peak because just one phonon is involved. In addition,

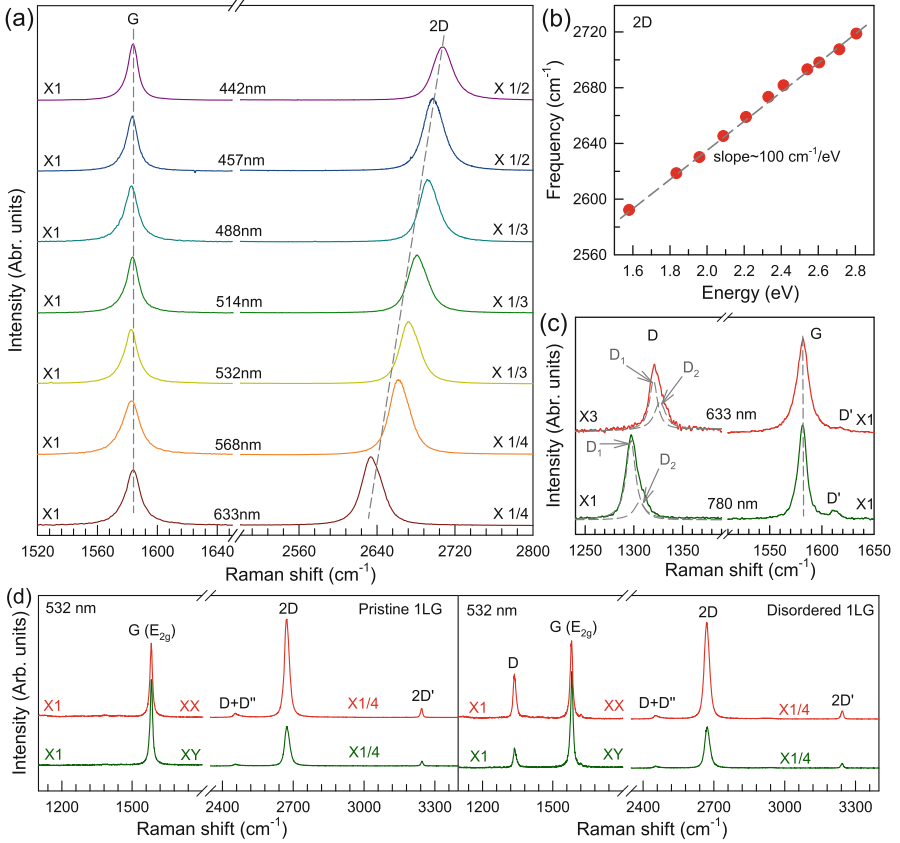


Fig. 1.4 (a) Raman spectra of 1LG measured at various excitations in the G and 2D spectral region. (b) 2D-peak position as a function of excitation energy, and the slope is $100 \text{ cm}^{-1}/\text{eV}$. (c) Comparison of Raman spectra with D, G and D bands under 633 and 780 nm excitations. The two components (D_1 and D_2) of Lorentzian fitting for the D band in graphene are shown. (d) Polarized Raman spectra of the pristine and disordered 1LG under 532 nm excitation. (Reproduced with permission from Ref. [9])

the intensities of the DR peaks are dependent on ε_L because of the ε_L -dependent photon absorption and electron-phonon coupling in the Raman scattering process [33]. Furthermore, the DR peaks of pristine and disordered 1LG show polarized behaviour, as shown in Fig. 1.2d, due to the selective optical absorption and emission mediated by electron-phonon coupling in the DR Raman process [33, 39].

Apart from graphene, the DR Raman process is also present in other graphene-based materials, such as graphite, carbon nanotubes and multilayer graphenes, although they do not have the linear band structures. Thus, phonons of graphene-based materials away from Γ can also be probed by Raman spectroscopy via the double resonant Raman process [32, 34, 35].

1.3 Raman Spectroscopy of Multilayer Graphene

1.3.1 Group Theory of AB-Stacked Multilayer Graphene

One of the prerequisites of the DR Raman process is the permission of the selection rules, including electron-photon and electron-phonon couplings. These selection rules are determined by group theory. The selection rule of electron-photon coupling is determined by the symmetries of the π electron and photon, and the selection rule of electron-phonon coupling is determined by the symmetries of the π electron and phonon. The symmetries of the electron and phonon can be obtained from space group analysis. Table 1.1 presents the space groups and wave-vector point groups for 1LG, AB-NLG, and graphite at the high symmetry points [11]. Because the phonon along the Γ -K axis is the main contribution of the DR process [33], the symmetry information of the Γ -K (T) axis is also shown.

The irreducible representations for the lattice vibrations (Γ_{vib}) of 1LG, even N layer graphene (ENLG) and odd N layer graphene (ONLG) at Γ and along the Γ -K axis in the BZ are found in Table 1.2. Both Bethe and Mulliken notations are adopted here for the phonon modes. A more complete group theory analysis at each high symmetry point inside the BZ and their N -dependent behaviour can be found in Ref. [41].

Momentum conservation makes phonons at Γ be observable in the first order Raman process. The phonon modes at Γ for 1LG, AB-2LG and AB-3LG are summarized with Mulliken notation:

$$\begin{aligned}\Gamma_{1LG} &= A_{2u} + B_{2g} + E_{1u} + E_{2g} \\ \Gamma_{AB-2LG} &= 2(A_{1g} + E_g + A_{2u} + E_u) \\ \Gamma_{AB-3LG} &= 2A'_1 + 4A''_2 + 4E' + 2E''\end{aligned}$$

Compared to 1LG, the G band in AB-2LG belongs to the E_g irreducible representation, which is doubly degenerate and represents the atomic motion of

Table 1.1 The space groups and wavevector point groups for NLG and graphite at all related points in the Brillouin zone

	Space group	Γ	K(K')	M	T(Γ -K)
1LG	$P6/mmm$	D_{6h}	D_{3h}	D_{2h}	C_{2v}
NLG even	$P\bar{3}m1$	D_{3d}	D_3	C_{2h}	C_2
NLG odd	$P\bar{6}m2$	D_{3h}	C_{3h}	C_{2v}	C_{1h}
Graphite	$P6_3/mmc$	D_{6h}	D_{3h}	D_{2h}	C_{2v}

Table 1.2 The irreducible representations for the lattice vibrations of 1LG, ENLG and ONLG at Γ and along the T(Γ -K) axis. Both Bethe and Mulliken notations are given

	1LG	ENLG	ONLG
Γ	$\Gamma_2^- + \Gamma_5^- + \Gamma_4^+ + \Gamma_6^+$ $A_{2u} + B_{2g} + E_{1u} + E_{2g}$	$N(\Gamma_1^+ + \Gamma_3^+ + \Gamma_2^- + \Gamma_3^-)$ $N(A_{1g} + E_g + A_{2u} + E_u)$	$(N-1)\Gamma_1^+ + (N+1)\Gamma_2^- + (N+1)\Gamma_3^+ + (N-1)\Gamma_3^-$ $(N-1)A'_1 + (N+1)A''_2 + (N+1)E' + (N-1)E''$
T(Γ -K)	$2T_1 + T_2 + 2T_3 + T_4$ $2A_1 + A_2 + 2B_1 + B_2$	$3N(T_1 + T_2)$ $3N(A+B)$	$(3N+1)T^+ + (3N-1)T^-$ $(3N+1)A' + (3N-1)A''$

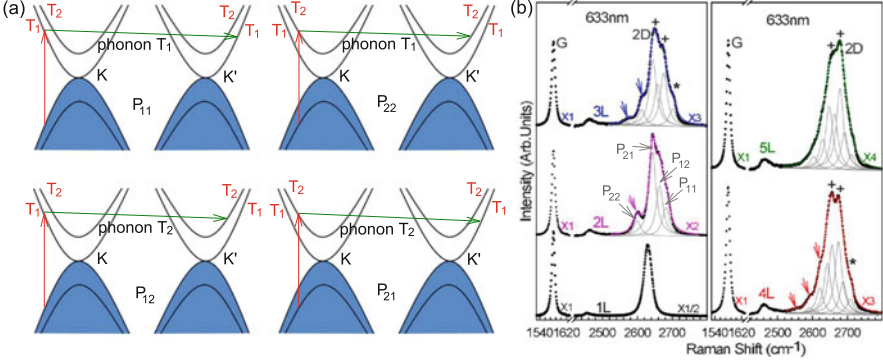


Fig. 1.5 (a) The four allowed DR processes in AB-2LG, denoted as P₁₁, P₂₂, P₁₂ and P₂₁. (b) Raman spectra of the G and 2D peaks for 1LG and AB-stacked 2-5LGs excited by a 633 nm laser. The 2D peaks are fitted by Lorentzian line shapes (gray peaks). The arrows, crosses and stars on the 2D peak indicate its weak shoulders at the low energy side, strongest components and weak shoulders at the high energy side, respectively. (Reproduced with permission from Ref. [22])

nearest neighbour carbon atoms moving against each other within the plane and in phase between the two layers, denoted as the symmetric G mode [11]. The E_u representation, which is not Raman active in AB-2LG because of the centre of inversion symmetry in the D_{3d} point group, can become Raman active if this inversion symmetry operation is broken by the presence of twisting stacking [42, 43], doping [22, 44, 45] and strain [46]. The E_u mode is also represented by the atomic motion of the nearest neighbour carbon atoms moving against each other within the plane but out-of-phase between the two layers, denoted as the antisymmetric G band [11]. There is also a low-frequency E_g mode (31 cm^{-1}), corresponding to the interlayer rigid shear vibration, the so-called C mode [26]. The other two A_{1g} irreducible representations are phonon modes at $\sim 90 \text{ cm}^{-1}$ (LB mode) and $\sim 867 \text{ cm}^{-1}$ [9]. For AB-3LG, the corresponding G and C bands should be assigned to E' and E'' , and the out-of-plane vibrational modes assigned to A'_1 and A''_2 .

1.3.2 Raman Spectra of AB-Stacked Multilayer Graphene

For intrinsic multilayer graphene, the characteristic G peak exhibits similar features located at $\sim 1582 \text{ cm}^{-1}$. However, the DR-related Raman peaks exhibit distinguishing properties from 1LG due to the different band structures in MLG. In the DR Raman process, the symmetry of electrons and phonons in MLG should be taken into account. Taking AB-2LG as an example, the number of allowed DR processes will be different from those in 1LG since both electronic and phonon branches are doubled. The transitions of $T_1 \rightleftharpoons T_2$ along the T axis in the BZ are allowed for AB-2LG, as shown in Fig. 1.5a [41]. The TO phonons for AB-2LG have T_1 and

T_2 symmetries. For the electron scattering by a T_1 phonon, the allowed process should occur in the K and K' electronic bands with the same symmetry, $T_1 \rightarrow T_1$ or $T_2 \rightarrow T_2$. However, the T_2 phonon connects conduction bands of different symmetries, i.e., $T_1 \rightleftharpoons T_2$. Thus, there are four possible DR processes, as shown in Fig. 1.5a.

Figure 1.5b shows Raman spectra of 1LG and AB-stacked 2-5LGs excited by a 633 nm laser. All the G peaks can be fitted by a single Lorentzian peak at $\sim 1582 \text{ cm}^{-1}$. 1LG has a single 2D peak at 2629.7 cm^{-1} . The 2D band of AB-2LG can be fitted by four Lorentzian peaks, corresponding to the four DR processes in Fig. 1.5a [13, 41]. For AB-3LG, the 2D bands are expected to consist of 15 Lorentzian peaks based on the symmetry analysis, and those of AB-4LG and AB-5LG are more complex [41]. However, the number of observed components is much less than the theoretical one because of the possible degeneracy and overlapping of these peak components. Six and eight components are sufficient to fit the 2D bands of AB-3LG and AB-4LG, respectively, in which the peak widths of all the components are kept as a fixed constant of 24 cm^{-1} [22]. As shown in Fig. 1.5b by arrows, crosses and stars, five and six 2D components can be clearly identified in the Raman spectra of AB-3LG and AB-4LG excited by the 633 nm laser, respectively. The 2D band of AB-4LG under 633 nm excitation shows more distinct spectral features than that under 532 nm excitation. AB-3LG and AB-4LG can be distinguished under 633 nm excitation by verifying the peak positions and number of shoulders at the lower energy side and the intensity ratio of the strongest two components of their 2D bands, as indicated by arrows and crosses in Fig. 1.5b. Thus, Raman spectroscopy can be used to clearly identify 1LG and AB-stacked 2-4LG under 633 nm excitation [22].

Now, we can present the detailed insights into the first order Raman scattering process in AB-NLG and graphite. In graphite, there are now two Raman-active E_{2g} modes, and each is doubly degenerate. The high-energy E_{2g} mode due to the in-plane vibrations is widely studied as the so-called G peak in all graphite systems [12, 13]. The low-frequency E_{2g} mode is the C mode, which results from the relative motion of atoms in the adjacent planes. There is no C mode in 1LG because there is only one layer. The C mode is observed at 43.5 cm^{-1} in bulk graphite, whose frequency is determined by the interlayer coupling force constant [28]. Figure 1.6a plots the C and G modes of AB-stacked 2-8LG and bulk graphite, while Fig. 1.6b shows Pos(C) and Pos(G) of AB-NLG as a function of $1/N$. The G peaks exhibits a Lorentzian lineshape, while the C mode displays an asymmetrical profile, which can be well fitted by the Breit-Wigner-Fano (simplified as Fano) lineshape, as shown in Fig. 1.6c for AB-3LG and bulk graphite. The unusual lineshape originates from the quantum interference between a Raman-active phonon and the continuum electronic transitions, as shown in Fig. 1.6d.

In contrast to the constant Pos(G) of $\sim 1582 \text{ cm}^{-1}$ in AB-NLG, Pos(C) decreases monotonously with decreasing N . The N -dependent Pos(C) in AB-NLG can be well explained by the linear chain model (LCM), [26] in which each graphene layer is considered as one ball for the rigid interlayer shear vibration and only the nearest-neighbour interlayer interactions are taken into account. There are $N-1$ pairs of

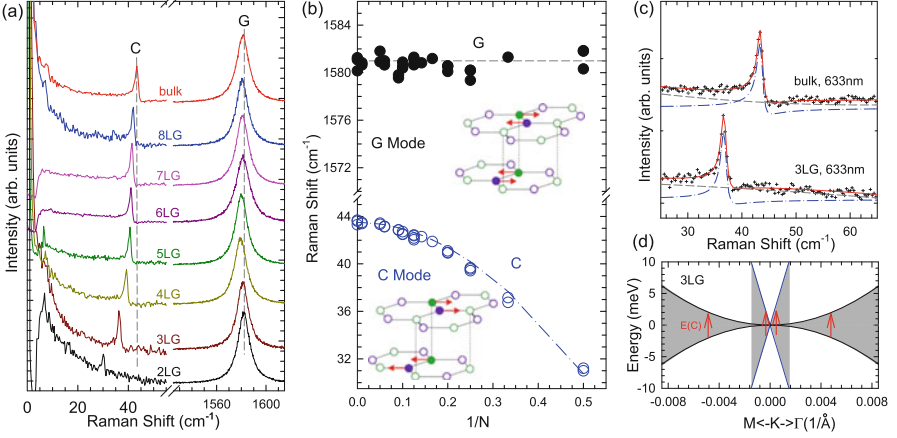


Fig. 1.6 (a) Raman spectra of the C and G peaks for AB-stacked 2-8LG and bulk graphite. The intensity of all the C modes is increased by 10 times. (b) Pos(G) and Pos(C) of AB-NLG as a function of $1/N$. The insets show the atomic displacements of the C and G modes. (c) The C peak of AB-3LG and bulk graphite fitted by the Fano lineshape. The solid lines, dash lines and dash-dot lines are the fitted curve, background and Fano component, respectively. (d) Schematic band structure of 3LG near the K point. The transitions denoted by arrows have the same energy as the C mode. (Reproduced with permission from Ref. [26])

degenerate C modes, denoted as C_{NN-i} , $i=1,2,\dots,N-1$. Here, the C mode with the highest frequency is assumed as C_{N1} ($i=N-1$), and the lowest one is C_{NN-1} ($i=1$). The interlayer shear coupling can be described by an interlayer force constant per unit area, α^{\parallel} . The frequencies ω (in cm^{-1}) and the displacement patterns of $N-1$ shear modes can be calculated by solving the corresponding $N \times N$ (tridiagonal) dynamical matrix as follows [42]:

$$(\omega_i)^2 \mathbf{u}_i = \frac{1}{2\pi^2 c^2 \mu} \mathbf{D} \mathbf{u}_i \quad (1.1)$$

where $\mu = 7.6 \times 10^{-27} \text{ kg}\text{\AA}^{-2}$ is the monolayer mass per unit area, \mathbf{u}_i is the phonon eigenvector of mode i with frequency ω_i , $c = 3.0 \times 10^{10} \text{ cm/s}$ is the speed of light and \mathbf{D} the shear part of the force constant matrix. Thus, the frequency of the C_{NN-i} mode can be given by [26]

$$\begin{aligned} \omega(C_{NN-i}) &= \frac{1}{\pi c} \sqrt{\alpha^{\parallel} / \mu \sin(i\pi/2N)} \\ &= \sqrt{2} \omega(C_{21}) \sin(i\pi/2N) \\ &= \omega(C_{bulk}) \sin(i\pi/2N), \end{aligned} \quad (1.2)$$

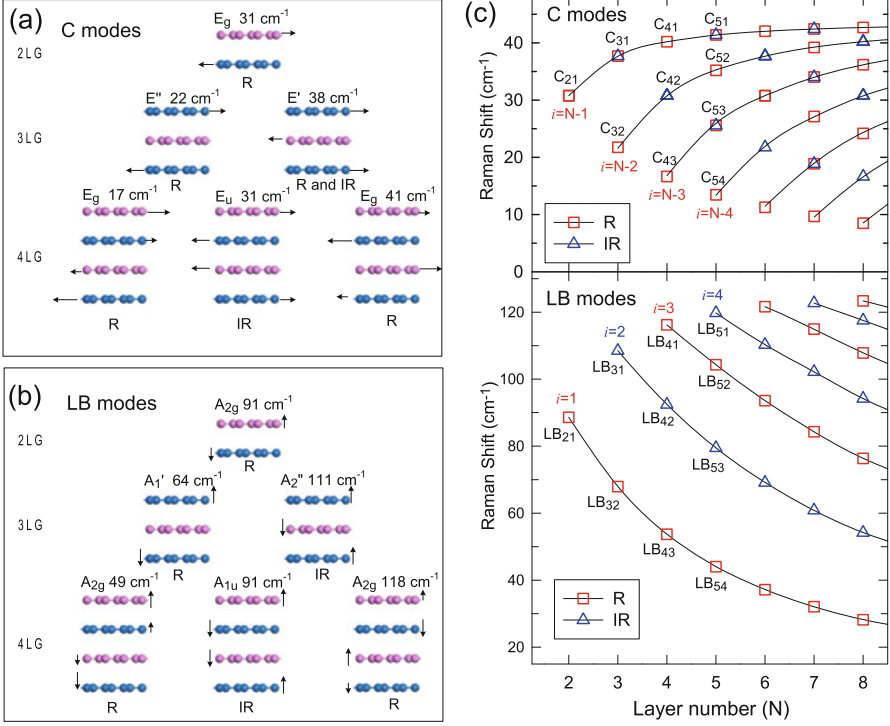


Fig. 1.7 Symmetry, frequency, Raman activity and normal mode displacement for each C mode (a) and LB mode (b) of AB-stacked (2–4)LG. (c) Pos(C) and Pos(LB) of AB- N LG as a function of N calculated by LCM and 2LCM, respectively. The rectangles and triangles indicate Raman (R) and infrared (IR) active modes, respectively

where $i=1, 2, \dots, N-1$. The relation of $\omega(C_{bulk}) = \sqrt{2}\omega(C_{21})$ is in line with the experimental results, $\text{Pos}(C) \sim 31 \text{ cm}^{-1}$ for AB-2LG and $\text{Pos}(C) \sim 43.5 \text{ cm}^{-1}$ for bulk graphite. Based on the experimental values of $\omega(C_{bulk})$ or $\omega(C_{21})$, we can obtain the only unknown parameter, the interlayer shear coupling strength $\alpha^{\parallel} \sim 12.8 \times 10^{18} \text{ N/m}^3$.

Figure 1.7a depicts the frequencies and the corresponding displacement patterns of $N-1$ C modes in AB- N LG ($N=2, 3, 4$). The C modes can be Raman-active (R), infrared-active (IR) or both, depending on the symmetry and N . As stated above, ENLG and ONLG belong to D_{3d} and D_{3h} , respectively [41, 47]. Thus, $N-1$ C modes in AB-stacked ENLG and ONLG are represented by $\frac{N}{2}E_g + \frac{N-2}{2}E_u$ and $\frac{N-1}{2}E'' + \frac{N-1}{2}E'$, respectively. E_g and E'' are Raman active, E_u is IR active and E' is both R and IR active. The detailed information of the assignments can be found in Ref. [47]. However, only the highest-frequency C modes were observed in the Raman spectra of AB-MLG (Fig. 1.6a). Other Raman active modes were not detected due to the weak electron-phonon coupling (EPC) and the unsuitable polarization configuration [26].

In AB-*N*LG, there is another interlayer mode, the LB mode, due to the relative motions of the adjacent layers perpendicular to the basic plane. Similar to the C modes, with a given N , there are $N-1$ LB modes, denoted as LB_{NN-i} , where $i = 1, 2, \dots, N-1$, in which the LB_{N1} represents the LB modes at the highest frequency. Unlike the C modes, the LB modes in AB- and ABC-stacked *N*LG cannot be observed at room temperature directly due to the weak EPC [26]. However, in twisted-*N*LG (t*N*LG), the LB modes can be detected under the resonance condition [27, 48, 49]. Replacing α^{\parallel} with the interlayer layer-breathing force constant α^{\perp} in Eq. 1.2, the corresponding Pos(LB) can be obtained. However, Wu *et al.* found that LCM underestimated the frequencies of the LB_{NN-i} ($i = 1, 2, \dots, N-2$) modes in t*N*LG, implying that the second nearest layer-breathing force constant (β^{\perp}) should be taken into account to reproduce the LB modes. Considering the first and second nearest interlayer coupling and then diagonalizing the corresponding $N \times N$ (tridiagonal) dynamical matrix addressed above (Eq. 1.2), we can obtain the frequencies and the displacement patterns for all the LB modes. This improved LCM is denoted as 2LCM [27]. The interlayer coupling in the perpendicular direction is determined, $\alpha^{\perp} \sim 106 \times 10^{18} \text{ N/m}^3$ and $\beta^{\perp} \sim 9.3 \times 10^{18} \text{ N/m}^3$ [27, 50]. Then $N-1$ LB modes are explicit, as shown in Fig. 1.7b, considering AB-(2–4)LG as examples. $N-1$ LB modes in AB-stacked ENLG and ONLG are represented by $\frac{N}{2}A_{2g} + \frac{N-2}{2}A_{1u}$ and $\frac{N-1}{2}A_2'' + \frac{N-1}{2}A_1'$, respectively, in which A_{2g} and A_1' are Raman active, while A_{1u} and A_2'' are IR active.

Figure 1.7c plots Pos(C) and Pos(LB) of AB-*N*LG as functions of N reproduced by LCM and 2LCM, respectively. The Raman-active and infrared-active modes are also identified. Overall, LCM and 2LCM can predict the N -dependent Pos(C) and Pos(LB) of AB-*N*LG, respectively. Furthermore, because Pos(C₂₁) and Pos(LB₂₁) are linked with the corresponding interlayer force constant between two adjacent layers, the good agreement between LCM/2LCM and experimental data for AB-*N*LG indicate a constant interlayer force constant from 2LG to bulk graphite. Moreover, 2LCM may only be suitable for one atom thickness 2D materials, such as graphene and BN; however, the LCM discussed above can be potentially applied to all 2d materials, such as MoS₂, WSe₂, black phosphorus (BP) and even 2d vdWHs [51–53]. Because the positions of the C and LB modes in 2DMs are strongly dependent on the layer number, the C and LB modes can be used for thickness identification of 2DMs [52–54].

1.3.3 Raman Spectra of ABC-Stacked Multilayer Graphene

In addition to N , the stacking order also has a great influence on the electrical and optical properties of *N*LG. Apart from the AB stacking, ABC (rhombohedral) stacking is also common in *N*LG. ABC-*N*LG comprises $\sim 15\%$ of the area in exfoliated samples, [55] which is in good agreement with a previous X-ray diffraction study of bulk graphite [56]. The Raman spectra of AB- and ABC-*N*LG

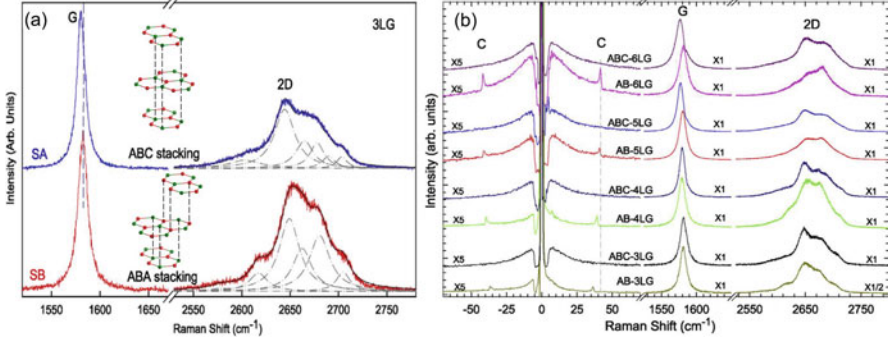


Fig. 1.8 (a) Raman spectra of 3LG measured at the ABA and ABC zones in the G and 2D mode regions. Schematic diagrams of ABA and ABC structures are shown. (b) Raman spectra of AB and ABC-stacked 3–6LG in the C, G and 2D peak spectral regions at room temperature. The C modes can be observed in AB-NLG, but not in ABC-NLG. (Reproduced with permission from Ref. [47])

are quite different from each other. $\text{Pos}(G)$ of ABC-NLG is $1\text{--}5\text{ cm}^{-1}$ lower than that of AB-NLG, depending on N [47]. The 2D mode profile of ABC-NLG shows distinct characteristics from those of AB-NLG, [47, 57–59] as shown in Fig. 1.8a for the case of 3LG, which is ascribed to the different electronic structures between them. As discussed above, six sub-peaks can be used to closely fit the 2D peak of AB-3LG, while the 2D mode of AB-3LG exhibits a more asymmetric feature. Further characterization of the 2D mode profile in ABC- and AB-stacked 4–6LG can be found in Refs. [47, 58, 59]. The differences in the 2D mode profiles between AB- and ABC-stacked NLG depend on the excitation energy (E_{ex}) and become more complicated with increasing N .

In the low frequency region, the C_{N1} modes can only be observed in AB-NLG at room temperature but not in ABC-NLG, [47] as shown in Fig. 1.8b. The absence of the C_{N1} mode in ABC-NLG was attributed to the Raman inactivity induced by the intrinsic symmetry and the weak EPC. Lui *et al.* observed the C_{31} mode at $\sim 33\text{ cm}^{-1}$ in AB-3LG and the C_{32} peak at $\sim 19\text{ cm}^{-1}$ in ABC-3LG suspended on quartz substrate at a high temperature of approximately 800 K by laser heating [58]. However, all the C_{NN-i} modes in ABC-NLG cannot be observed all the time on SiO_2/Si substrate, even when the laser power is as high as 10 mW, because a high substrate background emerges, [47] which is quite different from that on a quartz substrate [55]. The results showed that the C mode can also be utilized to identify AB and ABC stacking orders in NLG.

1.3.4 Raman Spectra of Twisted Multilayer Graphene

In addition to AB and ABC stacking orders, n LGs, m LGs, p LGs, ... (AB- n LG, AB- m LG, AB- p LG, ... if $n > 1, m > 1, p > 1, \dots, N = n + m + p + \dots$) can be stacked together with twist angles (θ_i) at each twist interface to form twisted N LG (tNLG, or $t(n+m+p+\dots)$ LG). For example, $t(m+n)$ LG is assembled by m LG ($m \geq 1$) and n LG ($n \geq 1$) flakes. Twisted graphene layers occur naturally at the surface of crystalline graphite, so that tNLG can be generated naturally by accidentally folding graphene layers onto themselves or other graphene flakes in the ME preparation process [42, 43]. tNLG has been widely observed to occur in non-controlled manner in graphene flakes grown by CVD [48, 49, 60–63]. The simplest tNLGs, twisted bilayer graphenes (t2LGs), can even exhibit novel physical properties due to the periodically modulated interaction between the two Dirac electron gases with a large Moiré supercell, as shown in Fig. 1.9a. They have a Dirac-like linear dispersion with

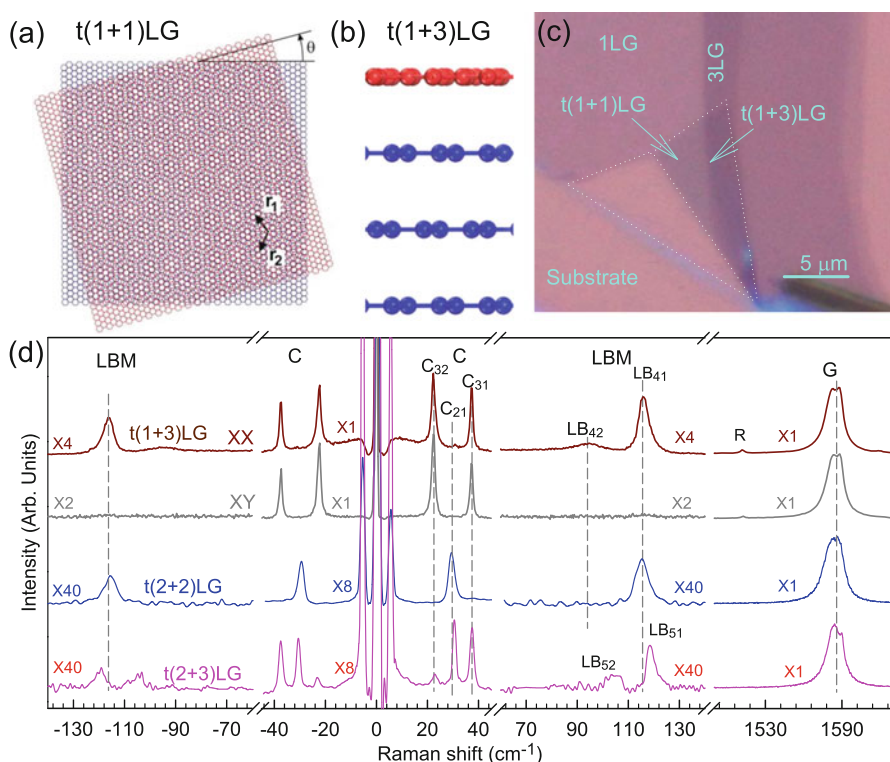


Fig. 1.9 (a) Moiré pattern of $t(1+1)$ LG. (b) Schematic diagram of $t(1+3)$ LG. (c) Optical image of a flake comprising $t(1+1)$ LG and $t(1+3)$ LG. (d) Stokes/anti-Stokes Raman spectra in the C and LB spectral range, and Stokes Raman spectra in the G peak region for $t(1+3)$ LG, $t(2+2)$ LG and $t(2+3)$ LG. Polarized Raman spectra of $t(1+3)$ LG are also shown. (Reproduced with permission from Ref. [42] and Ref. [27])

a Fermi velocity lower than that in 1LG [64]. By changing θ_t , it is possible to tune the optical absorption [65]. θ_t can be expressed in terms of the twist vector, [66, 67] (p, q), defined as the coordinates with respect to the basis vectors of 1LG. The positions of the so-called R and R' Raman bands have been used to probe θ_t in tNLG [48, 49, 68, 69].

In addition to θ_t , the stacking sequence is also important for modulating the physical properties in tNLG. For example, t(2+3)LG has significantly different properties compared to AB-5LG, t(1+4)LG, or t(1+1+3)LG, etc., even though all these have the same $N=5$. For a given total N , the choice of m, n , etc. (with $m+n+\dots=N$) and relative angles of each interface between m LG, n LG, ... leads to a family of systems with different optical and electronic properties [27, 42, 68, 69]. The band structure of t($m+n$)LG can be considered as the overlap between those of m LG and n LG. Figure 1.9b shows the diagram of t(1+3)LG, and Fig. 1.9c presents an optical image of t(1+1)LG and t(1+3)LG formed by the ME method.

From the perspective of the Raman spectroscopy of tNLG, several features are usually observed. The G peaks are usually significantly enhanced, and two further sub-peaks (G^+ and G^-) can be observed with the proper laser excitation if m LG ($m>1$) is one of the constituents [42, 43]. The enhancement of the G mode originates from the match between the excitation laser and energy gap of the van Hove singularities (VHSs) in the joint density of state (JDOS) of all the optically allowed transitions (JDOS_{OAT}) [42]. In the low-frequency region, tNLG also exhibits some distinguishing characteristics from AB-NLG. Because the twisted interface would obstruct the interlayer shear coupling due to the periodicity mismatch between the two twisted layers, the C modes locate in the AB-stacked constituent [42]. However, the twisted interface would not affect the interlayer breathing coupling; thus, the LB modes are from the collective motions of all the stacked layers [27]. Therefore, Pos(C) of tNLG is mainly determined by the layer number of each AB-stacked constituent, while its Pos(LB) is mainly determined by N , as shown in Fig. 1.9d. Most of the C modes and one or two LB modes can be observed under the resonant condition in t($m+n$)LG, because the twist-induced lower symmetry makes them Raman active [27, 42]. The N -dependent Pos(C) of AB-NLG can be predicted by LCM [26, 70]. However, in tNLG, a softening factor is introduced for the C mode at the twisted interface for shear coupling, $\alpha_t^\parallel/\alpha_0^\parallel \sim 0.2$, and another softening factor is considered at the AB-stacked interface next to the twist interface, $\alpha_{0t}^\parallel/\alpha_0^\parallel \sim 0.9$, producing the so-called twist LCM (tLCM) [42]. The 2LCM used in AB-NLG can be also adopted for tNLG [27]. tLCM and 2LCM can accurately reproduce the experimental Pos(C) and Pos(LB) in tNLG, respectively [27, 42].

1.4 Resonance Raman Spectroscopy of Monolayer and Multilayer Graphene

Raman scattering is a process related to the generation of electron-hole pairs by photon excitation, electron-phonon interaction, electron-hole recombination and photon emission. Thus, in addition to the selection rule and Raman tensor, the intensities and profiles of Raman modes are mainly determined by the EPC, electron-photon interaction and electronic band structure of solid materials. The intensity of the Raman mode in 1LG can be calculated by second order perturbation theory [33]. As discussed above, most of the Raman modes in graphene are involved in resonance Raman scattering because of the unique band structure [9]. Even the Raman intensity of the G mode, I(G), in 1LG is dominated by the quantum interference effect [15]. In AB-NLG, the quantum interference between the C mode and a continuum of electronic transitions near the K point plays an important role in the Fano lineshape of the C modes, [26] as shown in Fig. 1.6c, d. For tNLG, significant enhancements of first order modes (C, LB and G modes) are always observed when the laser excitation energy matches that of the VHSs in JDOS_{OAT} [42]. In the following subsections, we will discuss the three resonant Raman effects in 1LG and MLG.

1.4.1 Quantum Interference of the G and 2D Modes

In the DR process in Fig. 1.2, only the one-dimensional wave vectors are considered, which means that the wave vectors of the involved phonons or defects are always reversed (\mathbf{q} , $-\mathbf{q}$). A theoretical work found that the integration in the two-dimensional BZ does not alter the DR phonon wave vectors determined from the one-dimensional integration [71]. This is because, when the wave vectors of involved phonons or defect are not reversed, the contribution of two wave vectors would be cancelled by interference. In particular, when the two wave vectors are in the same direction, the contribution could be almost totally destructive interference. Thus, it is reasonable to describe the DR process by the one-dimensional model.

The quantum interference of the G mode was first predicted by theory, [16] and then proven by an electrostatic doping experiment [15]. Under electrostatic doping, I(G) increases dramatically. This unexpected phenomenon presents evidence of a new understanding of resonance Raman scattering in graphene. Figure 1.10a shows I(G) as a function of $2|E_F|$, where E_F is the Fermi level of graphene tuned by the electrostatic doping. The observation cannot be interpreted well by the general assumption that the pathway of G mode Raman scattering is only on resonance (I in Fig. 1.10a). To further understand the phenomenon, pathways are extended that can be close to resonance (II in Fig. 1.10a) and off resonance. In this condition, all pathways interfering with each other have different quantum mechanical amplitudes, including phase and magnitude. For any specific one-

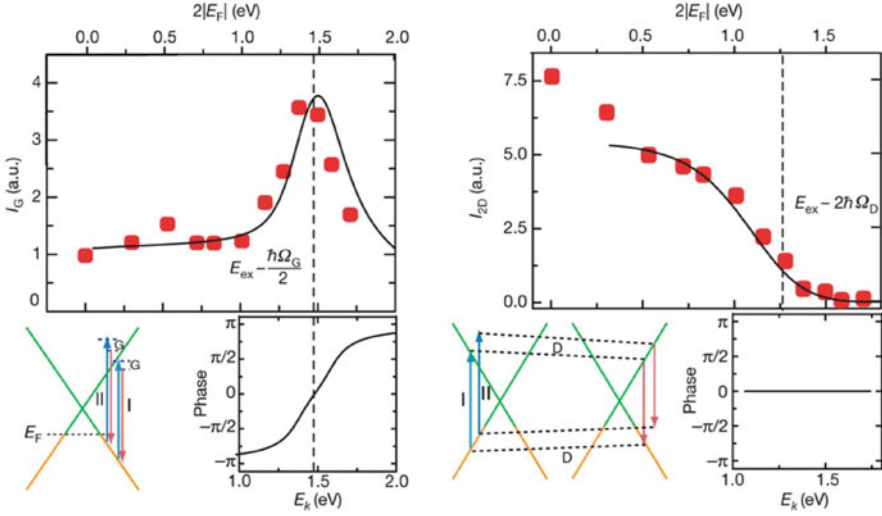


Fig. 1.10 Upper panel: Doping dependence of $I(G)$ (left) and $I(2D)$ (right). The black solid line is the theoretical prediction. Lower left panel: schematic of two representative pathways (I and II) of the G mode through two different intermediate excited states and the quantum phase of Raman pathway for the G mode as a function of intermediate excitation energy. Lower right panel: schematic of two representative pathways (I and II) of the 2D mode through two different intermediate excited states and the quantum phase of Raman pathway for the 2D mode as a function of intermediate excitation energy. (Reproduced with permission from Ref. [15])

phonon and one-photon state, $I(G)$ is described by

$$I(G) = \left| \sum_k C_k R_k \right|^2 \quad (1.3)$$

$$R_k = \frac{1}{(E_{ex} - E_k - i\gamma)(E_{ex} - \hbar\omega_G - E_k - i\gamma)}$$

where C_k and R_k are the matrix element and resonance factor, respectively. Its phase $\omega = \arg(R_k)$ is plotted as a function of transition energy (E_k) in Fig. 1.10a. With E_k above and below the energy of $E_{ex} - \hbar\omega_G/2$, the pathways have a phase difference of approximately π . With a small enough $|E_F|$, all pathways are allowed and interfere destructively. With a large enough $|E_F|$, all pathways are blocked. The two situations lead to a weak overall Raman signal. When $2|E_F| = E_{ex} - \hbar\omega_G/2$, $I(G)$ reaches a maximum value because just half of the transitions with the same phase sign (positive or negative) are allowed, and destructive interference would not occur. In addition to the G mode, $I(2D)$ is also determined by the quantum interference effect. The different pathways have the same phase, presented in Fig. 1.10b, resulting in the monotonic decrease of $I(2D)$.

1.4.2 Fano Resonance of the C and G Mode in Multilayer Graphene

The C modes of the Raman spectrum in AB-NLG exhibit a Fano lineshape, [26] as shown in Fig. 1.6c. Historically, the Fano lineshape was observed in the Raman spectra of several systems, such as degenerate silicon systems, [72] metallic carbon nanotubes, [73], nanowires, [74] topological insulators [75] and 2d semiconductors [76]. The Fano lineshape of a Raman mode can be expressed by [26]

$$I(\omega) = I_0 \frac{[1 + 2(\omega - \omega_0)/(q\Gamma)]^2}{[1 + 4(\omega - \omega_0)^2/\Gamma^2]} \quad (1.4)$$

where I_0 , ω_0 , Γ and $1/|q|$ are the intensity, uncoupled mode frequency, broadening parameters and coupling coefficient, respectively. The peak maximum is at $\omega_{max} = \omega_0 + \Gamma/2q$, while the full-width at half-maximum (FWHM) is $\Gamma(q^2+1)/|q^2 - 1|$. The Fano lineshape exhibits high asymmetry dependent on the coupling coefficient. It will recover to a Lorentzian lineshape when $1/|q|$ approaches to 0. Because Pos(G) remains constant and the C peak at 77 K has the same coupling coefficient, $1/|q|$, as that at room temperature, [26] the laser-induced electron-hole plasma and the multiphonon resonance can be ruled out as the reason for the resulting Fano lineshape. In general, the Fano lineshape of the C mode in AB-NLG can be attributed to the quantum interference between the C mode and a continuum of electronic transitions near the K point [26]. As in the case of AB-3LG in Fig. 1.6d, the C phonon can efficiently couple with the active electronic transitions with energies close to the C mode energy ($E(C)$, ~ 5 meV). The charge transferred from the substrate and the air molecules can raise the Fermi level (especially for $E_F > E(C)/2$). This can largely reduce the coupling coefficient of the Fano resonance, particularly for few-layer graphenes, which has been confirmed by the N -dependent $1/|q|$ [26].

The G band of 1LG should exhibit an asymmetric Fano-like lineshape near the charge neutrality point, whereas the line shape is symmetric when the graphene flake is doped by electrons or holes [77]. However, the G band of AB-2LG does not exhibit any Fano resonance, regardless of doping. The Fano resonance observed in the G band lineshape of 1LG originates from the interferences between the phonon and excitonic many-body spectra, whereas the absence of a Fano resonance in the G band lineshape of AB-2LG can be elucidated by the unexpected excitonic interaction in AB-2LG [77, 78]. However, compared with the imperceptible asymmetric C modes with $1/|q| \sim 0.3$, [26] the lineshape of the G mode in neutral 1LG just shows a very slightly asymmetric behaviour due to the much smaller $1/|q|$ of ~ 0.07 [77]. The Fano resonance of the G mode can also be observed in the infrared spectra of phonons in NLG because of the strong coupling between phonons and interband electronic transitions [79].

1.4.3 Resonance Raman Spectroscopy of Twisted Multilayer Graphene

The band structure of tNLG can be modified by several twist-related parameters, such as the layer number of the constituents and the twist angles, showing novel and interesting optical properties [42]. For example, the intensity of the first order modes can be enhanced strongly. As shown in Fig. 1.11a, the Raman signals of t(1+1)LG would be enhanced when E_{ex} matches its θ_t -dependent VHS energies of $JDOS_{OAT}$ [60, 61]. The relationship between the VHS energy of $JDOS_{OAT}$ and θ_t can be estimated by the formula [61] $E_{VHS} \approx 4\pi\theta_t\hbar v_f/\sqrt{3}a$, where a is the lattice constant of graphene (2.46 Å), \hbar is the reduced Planck's constant, and v_f is the Fermi velocity of 1LG (10^6 m/s). $JDOS_{OAT}$ of NLG can be calculated by the following equation [42]:

$$JDOS_{OAT}(E) \propto \sum_{ij} \sum_{\mathbf{k}} |M_{ij}(\mathbf{k})|^2 \delta(E_{ij}(\mathbf{k}) - E), \quad (1.5)$$

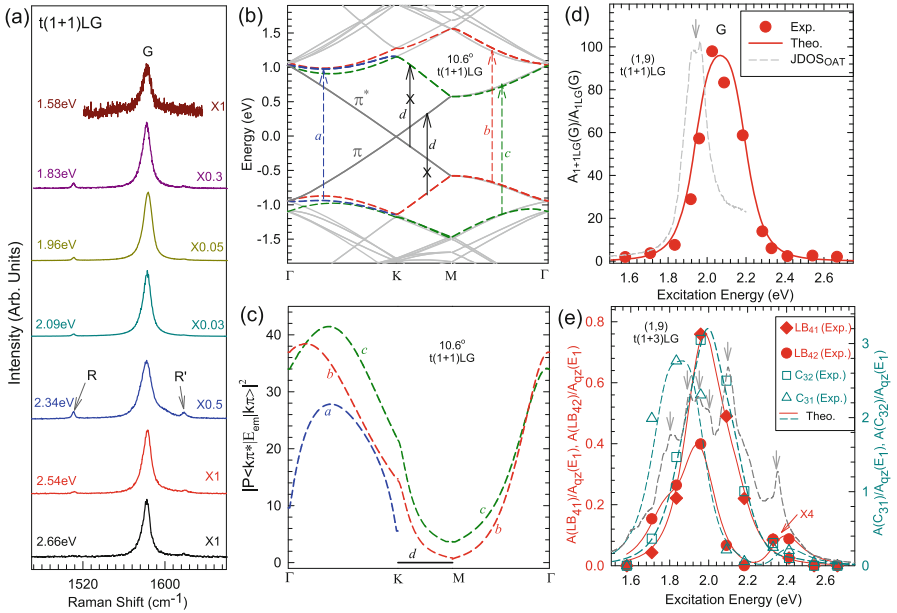


Fig. 1.11 (a) G mode of t(1+1)LG for seven E_{ex} . The R and R' modes are indicated by arrows. (b) The band structure of (1,9) t(1+1)LG. The optically allowed transitions are marked by dashed arrows, and the forbidden transitions are indicated by solid arrows with crosses. (c) Squared optical matrix elements of the corresponding band pairs in (b). (d) $A(\mathbf{G})$ of t(1+1)LG and (e) $A(C_{31})$, $A(C_{32})$, $A(LB_{41})$ and $A(LB_{42})$ of t(1+3)LG as a function of E_{ex} . The dashed lines indicated with arrows in (d) and (e) are $JDOS_{OAT}$ in t(1+1)LG and t(1+3)LG along Γ -K-M- Γ , respectively. (Reproduced with permission from Ref. [42])

where $M_{ij}(\mathbf{k})$ is the optical matrix element between the i th conduction and j th valence bands, and $E_{ij}(\mathbf{k})$ gives the transition energy of an $i \rightarrow j$ band pair at the wavevector \mathbf{k} . The band structure of t(1+1)LG with 10.6° ($(p,q)=(1,9)$) is shown in Fig. 1.11b, and the optically allowed transitions are marked by dashed arrows. The squared optical matrix elements of the corresponding transitions are shown in Fig. 1.11c. JDOS_{OAT} for t(1+1)LG is shown in Fig. 1.11d by dashed lines indicated with arrows, showing only one distinct VHS in JDOS_{OAT} labelled by arrows. The major contribution to the Raman intensity comes from the term of Eq. 1.5 when E_{ex} matches the VHS energies of JDOS_{OAT} . Therefore, the intensity of Raman modes in t($m+n$)LG as a function of E_{ex} can be evaluated by second order perturbation theory [33, 68],

$$A \propto \left| \sum_j \frac{M_j}{(E_{ex} - E_{VHS}(j) - i\gamma)(E_{ex} - E_{ph} - E_{VHS}(j) - i\gamma)} \right|^2, \quad (1.6)$$

where M_j are constants treated as fitting parameters that encompass the product of the electron-phonon and electron-phonon interaction matrix elements for the j th VHS in JDOS_{OAT} , E_{ph} is the phonon energy, and γ gives the energy uncertainty related to the lifetime of the excited state. Here, we adopt $\gamma = 0.15$ eV to reflect the effect of summation along all the high symmetry path. The E_{ex} -dependent G mode area intensity ($A(G)$) of t(1+1)LG is shown in Fig. 1.11d. The calculated results are in agreement with the experimental data.

In t(1+1)LGs, the VHS energy of the electronic density of states (DOS) is similar to that of JDOS , due to the simple band structure [42, 61]. Therefore, the resonant excitation energy can be estimated from the VHS energy of either DOS or JDOS . However, in t($m+n$)LG ($m \geq 1, n > 1$), the resonance process is more complicated because of its more complex band structure and EPC. More VHS energies exist in JDOS_{OAT} . Taking the (1,9) t(1+3)LG as an example, the E_{ex} -dependent $A(C)$, $A(LB)$ and $A(G)$ fitted by the VHS energies are in good agreement with the experimental data, [42] as shown in Fig. 1.11e.

Moreover, the DR process in t(1+1)LG is much more complicated, due to the folding of the band structure. Similar to 1LG, the 2D peak of most t(1+1)LGs exhibits a single Lorentzian peak. The FWHM, frequency and area of the 2D peak in t(1+1)LG depend on θ_t [61, 80]. Therefore, the profile of the 2D peak is not suitable for identifying the N of tNLG.

1.5 Conclusion

Graphene and MLG have extraordinary electronic, optoelectronic and mechanical properties as well as appealing applications in devices. In this chapter, we have reviewed the basic Raman spectroscopy of pristine 1LG and MLG, including the origin of the G mode; all the dispersive Raman modes in intrinsic 1LG; novel

Raman modes and new phenomena found in AB-, ABC- and twisted-MLG; how the layer number, stacking sequences and twist angle affect the Raman spectra of the C, LB and 2D modes; and the peculiar resonance Raman effects in pristine 1LG and MLG. The related Raman concepts reviewed for 1LG and MLG, such as the double resonance Raman spectroscopy, low-frequency interlayer Raman modes and the linear chain model, may be applicable to other 2DMs to understand the interlayer coupling in 2DMs. This chapter may be helpful to gain a deeper understanding of the Raman scattering process in various 2DMs.

Acknowledgements We acknowledge support from the National Key Research and Development Program of China (Grant No. 2016YFA0301204), the National Natural Science Foundation of China (Grant No. 11474277, 11874350 and 11434010), and the Beijing Municipal Science and Technology Commission.

References

1. K.S. Novoselov, A.K. Geim, S.V. Morozov, D. Jiang, Y. Zhang, S.V. Dubonos, I.V. Grigorieva, A.A. Firsov, *Science* **306**(5696), 666 (2004)
2. S. Laili, L. Henrard, *Phys. Rev. Lett.* **97**(3), 036803 (2006)
3. K.S. Novoselov, D. Jiang, F. Schedin, T.J. Booth, V.V. Khotkevich, S.V. Morozov, A.K. Geim, *P. Natl. Acad. Sci. USA* **102**, 10451 (2005)
4. X. Li, W. Cai, J. An, S. Kim, J. Nah, D. Yang, R. Piner, A. Velamakanni, I. Jung, E. Tutuc, et al., *Science* **324**(5932), 1312 (2009)
5. A. Reina, X. Jia, J. Ho, D. Nezich, H. Son, V. Bulovic, M.S. Dresselhaus, J. Kong, *Nano Lett.* **9**(1), 30 (2008)
6. A.K. Geim, K.S. Novoselov, *Nat. Mater.* **6**(3), 183 (2007)
7. A.K. Geim, I.V. Grigorieva, *Nature* **499**(7459), 419 (2013)
8. K.S. Novoselov, A. Mishchenko, A. Carvalho, A.H.C. Neto, *Science* **353**, 6298 (2016)
9. J.B. Wu, M.L. Lin, X. Cong, H.N. Liu, P.H. Tan, *Chem. Soc. Rev.* **47**, 1822 (2018)
10. H. Li, J.B. Wu, F. Ran, M.L. Lin, X.L. Liu, Y. Zhao, X. Lu, Q. Xiong, J. Zhang, W. Huang, H. Zhang, P.H. Tan, *ACS Nano* **11**, 11714 (2017)
11. L. Malard, M. Pimenta, G. Dresselhaus, M. Dresselhaus, *Phys. Rep.* **473**(5), 51 (2009)
12. A.C. Ferrari, D.M. Basko, *Nat. Nanotechnol.* **8**(4), 235 (2013)
13. A. Ferrari, J. Meyer, V. Scardaci, C. Casiraghi, M. Lazzeri, F. Mauri, S. Piscanec, D. Jiang, K. Novoselov, S. Roth, et al., *Phys. Rev. Lett.* **97**(18), 187401 (2006)
14. L. Malard, J. Nilsson, D. Elias, J. Brant, F. Plentz, E. Alves, A.C. Neto, M. Pimenta, *Phys. Rev. B* **76**(20), 201401 (2007)
15. C.F. Chen, C.H. Park, B.W. Boudouris, J. Horng, B. Geng, C. Girit, A. Zettl, M.F. Crommie, R.A. Segalman, S.G. Louie, et al., *Nature* **471**(7340), 617 (2011)
16. D. Basko, *New J. Phys.* **11**(9), 095011 (2009)
17. D. Yoon, H. Moon, Y.W. Son, J.S. Choi, B.H. Park, Y.H. Cha, Y.D. Kim, H. Cheong, *Phys. Rev. B* **80**(12), 125422 (2009)
18. A.C. Neto, F. Guinea, N.M. Peres, K.S. Novoselov, A.K. Geim, *Rev. Mod. Phys.* **81**(1), 109 (2009)
19. J.M. Dawlaty, S. Shivaraman, J. Strait, P. George, M. Chandrashekhara, F. Rana, M.G. Spencer, D. Veksler, Y. Chen, *Appl. Phys. Lett.* **93**(13), 131905 (2008)
20. P. Blake, E. Hill, A.C. Neto, K. Novoselov, D. Jiang, R. Yang, T. Booth, A. Geim, *Appl. Phys. Lett.* **91**(6), 063124 (2007)

21. X.L. Li, X.F. Qiao, W.P. Han, Y. Lu, Q.H. Tan, X.L. Liu, P.H. Tan, *Nanoscale* **7**(17), 8135 (2015)
22. W. Zhao, P. Tan, J. Zhang, J. Liu, *Phys. Rev. B* **82**(24), 245423 (2010)
23. M. Lazzeri, C. Attaccalite, L. Wirtz, F. Mauri, *Phys. Rev. B* **78**(8), 081406 (2008)
24. P. Tan, C. Hu, J. Dong, W. Shen, B. Zhang, *Phys. Rev. B* **64**(21), 214301 (2001)
25. S. Reich, C. Thomsen, *Philos. Transact. A Math Phys. Eng. Sci.* **362**(1824), 2271 (2004)
26. P. Tan, W. Han, W. Zhao, Z. Wu, K. Chang, H. Wang, Y. Wang, N. Bonini, N. Marzari, N. Pugno, et al., *Nat. Mater.* **11**(4), 294 (2012)
27. J.B. Wu, Z.X. Hu, X. Zhang, W.P. Han, Y. Lu, W. Shi, X.F. Qiao, M. Ijias, S. Milana, W. Ji, et al., *ACS Nano* **9**(7), 7440 (2015)
28. P.H. Tan, J.B. Wu, W.P. Han, W.J. Zhao, X. Zhang, H. Wang, Y.F. Wang, *Phys. Rev. B* **89**(23), 235404 (2014)
29. D. L. Nika, A. A. Balandin, *J. Phys. Condes. Matter* **24**, 233203 (2012)
30. M. Mohr, J. Maultzsch, E. Dobardžić, S. Reich, I. Milošević, M. Damnjanović, A. Bosak, M. Krisch, C. Thomsen, *Phys. Rev. B* **76**(3), 035439 (2007)
31. S. Siebentritt, R. Pues, K.H. Rieder, A.M. Shikin, *Phys. Rev. B* **55**(12), 7927 (1997)
32. R. Saito, A. Jorio, A. Souza Filho, G. Dresselhaus, M. Dresselhaus, M. Pimenta, *Phys. Rev. Lett.* **88**(2), 027401 (2001)
33. P. Venezuela, M. Lazzeri, F. Mauri, *Phys. Rev. B* **84**(3), 035433 (2011)
34. P. Tan, L. An, L. Liu, Z. Guo, R. Czerw, D.L. Carroll, P.M. Ajayan, N. Zhang, H. Guo, *Phys. Rev. B* **66**(24), 245410 (2002)
35. C. Thomsen, S. Reich, *Phys. Rev. Lett.* **85**(24), 5214 (2000)
36. P. Tan, Y. Deng, Q. Zhao, *Phys. Rev. B* **58**(9), 5435 (1998)
37. P. May, M. Lazzeri, P. Venezuela, F. Herziger, G. Callsen, J.S. Reparaz, A. Hoffmann, F. Mauri, J. Maultzsch, *Phys. Rev. B* **87**(7), 075402 (2013)
38. D. Basko, S. Piscanec, A. Ferrari, *Phys. Rev. B* **80**(16), 165413 (2009)
39. D. Yoon, H. Moon, Y.W. Son, G. Samsonidze, B.H. Park, J.B. Kim, Y. Lee, H. Cheong, *Nano Lett.* **8**(12), 4270 (2008)
40. S. Piscanec, M. Lazzeri, F. Mauri, A. Ferrari, J. Robertson, *Phys. Rev. Lett.* **93**(18), 185503 (2004)
41. L. Malard, M. Guimaraes, D. Mafra, A. Jorio, *Phys. Rev. B* **79**(12), 125426 (2009)
42. J.B. Wu, X. Zhang, M. Ijäs, W.P. Han, X.F. Qiao, X.L. Li, D.S. Jiang, A.C. Ferrari, P.H. Tan, *Nat. Commun.* **5**, 5309 (2014)
43. C. Cong, T. Yu, *Nat. Commun.* **5**, 4709 (2014)
44. L. Malard, D. Elias, E. Alves, M. Pimenta, *Phys. Rev. Lett.* **101**(25), 257401 (2008)
45. W. Zhao, P.H. Tan, J. Liu, A.C. Ferrari, *J. Am. Chem. Soc.* **133**(15), 5941 (2011)
46. J. Zabel, R.R. Nair, A. Ott, T. Georgiou, A.K. Geim, K.S. Novoselov, C. Casiraghi, *Nano Lett.* **12**(2), 617 (2012)
47. X. Zhang, W.P. Han, X.F. Qiao, Q.H. Tan, Y.F. Wang, J. Zhang, P.H. Tan, *Carbon* **99**, 118 (2016)
48. J.B. Wu, H. Wang, X.L. Li, H. Peng, P.H. Tan, *Carbon* **110**, 225 (2016)
49. M.L. Lin, T. Chen, W. Lu, Q.H. Tan, P. Zhao, H.T. Wang, Y. Xu, P.H. Tan, *J. Raman Spectrosc.* **49**, 46 (2018)
50. H. Wang, M. Feng, X. Zhang, P.H. Tan, Y. Wang, *J. Phys. Chem. C* **119**(12), 6906 (2015)
51. X. Zhang, X.F. Qiao, W. Shi, J.B. Wu, D.S. Jiang, P.H. Tan, *Chem. Soc. Rev.* **44**(9), 2757 (2015)
52. X.L. Li, W.P. Han, J.B. Wu, X.F. Qiao, J. Zhang, P.H. Tan, *Adv. Funct. Mater.* **27**(19), 1604468 (2017)
53. L. Liang, J. Zhang, B.G. Sumpter, Q. Tan, P.H. Tan, V. Meunier, *ACS Nano* **11**(12), 11777 (2017)
54. X.F. Qiao, X.L. Li, X. Zhang, W. Shi, J.B. Wu, T. Chen, P.H. Tan, *Appl. Phys. Lett.* **106**(22), 223102 (2015)
55. C.H. Lui, Z. Ye, C. Keiser, E.B. Barros, R. He, *Appl. Phys. Lett.* **106**(4), 041904 (2015)
56. H. Wilhelm, B. Croset, G. Medjahdi, *Carbon* **45**(12), 2356 (2007)

57. C. Cong, T. Yu, K. Sato, J. Shang, R. Saito, G.F. Dresselhaus, M.S. Dresselhaus, *ACS Nano* **5**(11), 8760 (2011)
58. C.H. Lui, Z. Li, Z. Chen, P.V. Klimov, L.E. Brus, T.F. Heinz, *Nano Lett.* **11**(1), 164 (2010)
59. T. Nguyen, J. Lee, D. Yoon, H. Cheong, *Sci. Rep.* **4**, 4630 (2014)
60. R.W. Havener, H. Zhuang, L. Brown, R.G. Hennig, J. Park, *Nano Lett.* **12**(6), 3162 (2012)
61. K. Kim, S. Coh, L.Z. Tan, W. Regan, J.M. Yuk, E. Chatterjee, M. Crommie, M.L. Cohen, S.G. Louie, A. Zettl, *Phys. Rev. Lett.* **108**(24), 246103 (2012)
62. J. Campos-Delgado, L.G. Cançado, C.A. Achete, A. Jorio, J.P. Raskin, *Nano Res.* **6**(4), 269 (2013)
63. A. Jorio, L.G. Cançado, *Solid State Commun.* **175**, 3 (2013)
64. Z. Ni, Y. Wang, T. Yu, Y. You, Z. Shen, *Phys. Rev. B* **77**(23), 235403 (2008)
65. P. Moon, M. Koshino, *Phys. Rev. B* **87**(20), 205404 (2013)
66. G. Trambly de Laissardière, D. Mayou, L. Magaud, *Nano Lett.* **10**(3), 804 (2010)
67. K. Sato, R. Saito, C. Cong, T. Yu, M.S. Dresselhaus, *Phys. Rev. B* **86**(12), 125414 (2012)
68. V. Carozo, C. Almeida, B. Fragneaud, P. Bedê, M. Moutinho, J. Ribeiro-Soares, N. Andrade, A. Souza Filho, M. Matos, B. Wang, et al., *Phys. Rev. B* **88**(8), 085401 (2013)
69. V. Carozo, C.M. Almeida, E.H. Ferreira, L.G. Cançado, C.A. Achete, A. Jorio, *Nano Lett.* **11**(11), 4527 (2011)
70. X. Zhang, W. Han, J. Wu, S. Milana, Y. Lu, Q. Li, A. Ferrari, P. Tan, *Phys. Rev. B* **87**(11), 115413 (2013)
71. J. Maultzsch, S. Reich, C. Thomsen, *Phys. Rev. B* **70**(15), 155403 (2004)
72. F. Cerdeira, T. Fjeldly, M. Cardona, *Phys. Rev. B* **8**(10), 4734 (1973)
73. H. Lin, L.A. Wray, Y. Xia, S. Xu, S. Jia, R.J. Cava, A. Bansil, M.Z. Hasan, *Nat. Mater.* **9**(7), 546 (2010)
74. R. Gupta, Q. Xiong, C. Adu, U. Kim, P. Eklund, *Nano Lett.* **3**(5), 627 (2003)
75. J. Zhang, Z. Peng, A. Soni, Y. Zhao, Y. Xiong, B. Peng, J. Wang, M.S. Dresselhaus, Q. Xiong, *Nano Lett.* **11**(6), 2407 (2011)
76. Q.H. Tan, Y.J. Sun, X.L. Liu, Y. Zhao, Q. Xiong, P.H. Tan, J. Zhang, *2D Mater.* **4**(3), 031007 (2017)
77. D. Yoon, D. Jeong, H.J. Lee, R. Saito, Y.W. Son, H.C. Lee, H. Cheong, *Carbon* **61**, 373 (2013)
78. E.H. Hasdeo, A.R. Nugraha, M.S. Dresselhaus, R. Saito, *Phys. Rev. B* **90**(24), 245140 (2014)
79. T.T. Tang, Y. Zhang, C.H. Park, B. Geng, C. Girit, Z. Hao, M.C. Martin, A. Zettl, M.F. Crommie, S.G. Louie, et al., *Nat. Nanotechnol.* **5**(1), 32 (2010)
80. R. He, T.F. Chung, C. Delaney, C. Keiser, L.A. Jauregui, P.M. Shand, C. Chancey, Y. Wang, J. Bao, Y.P. Chen, *Nano Lett.* **13**(8), 3594 (2013)